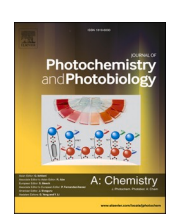
FISEVIER

Contents lists available at ScienceDirect

Journal of Photochemistry & Photobiology, A: Chemistry

journal homepage: www.elsevier.com/locate/jphotochem



Transition metal-doped CuO nanosheets for enhanced visible-light photocatalysis

Tank R. Seling ^{a,1}, Rowan R. Katzbaer ^{b,1}, Katherine L. Thompson ^{b,1}, Sophia E. Aksoy ^b, Basant Chitara ^a, Amit K. Shringi ^a, Raymond E. Schaak ^b, Ufana Riaz ^{a,*}, Fei Yan ^{a,*}

ARTICLE INFO

Keywords: CuO nanosheets Methylene blue Malachite green Visible-light photocatalysis

ABSTRACT

Herein, we report a comprehensive investigation of Zn- and Fe-doped CuO nanosheets as promising photocatalysts for the degradation of organic dyes. These nanosheets were synthesized via a hydrothermal process and thoroughly characterized through spectroscopic and microscopic techniques. Photocatalytic degradation experiments using methylene blue (MB) and malachite green (MG) revealed a marked increase in efficiency within the doped CuO nanosheets when compared to their undoped counterparts. The degradation kinetics showed MB following a zero-order model and MG following a first-order model. In particular, Zn and Fe-doped CuO nanosheets outperformed undoped CuO, degrading 66% and 73% of MB and 85% and 90% of MG within specific timeframes, while undoped CuO achieved 62% and 76% degradation, respectively. Computational analysis conducted with Gaussian 09 software pinpointed reactive sites susceptible to radical and electrophilic attacks in the dyes. The enhanced performance is credited to transition metal doping, which induces a red shift in the optical band gap, thereby improving visible light absorption and diminishing electron-hole recombination. This study underscores the potential of transition metal doping in bandgap engineering for efficient visible light-assisted photocatalytic remediation.

1. Introduction

Heterogeneous photocatalysis holds great promise as a method for degrading persistent organic pollutants (POPs) using semiconducting materials that are activated by light. When photons are absorbed, electron-hole pairs are formed, generating reactive species that break down contaminants into less toxic substances. Several materials, including titanium dioxide (TiO2) [1,2], zinc oxide (ZnO) [3,4], and graphitic carbon nitride (C_3N_4) – based nanostructures [5,6], have demonstrated effectiveness in this process. The efficiency of degradation is influenced by factors such as the choice of catalyst, pollutant concentration, pH, and light conditions. Despite remaining challenges, photocatalysis provides a sustainable approach for environmental remediation.

CuO nanostructures, which are photoactive with a high surface area, have applications in photocatalysis [7,8], solar energy devices [9,10], and electrode materials [11,12]. CuO is a p-type semiconductor with

bandgap in the range of 1.2–2.1 eV and it has been extensively utilized in the photocatalytic degradation of organic pollutants [13]. The wide range of the band gap usually arises due to the presence of defects, self-assembled morphologies like nanospheres, nanotubes, and nanosheets, as well as the presence of dopants. Many of the recent advances in the removal of organic pollutants with CuO have focused on composite materials. *Liu et al.* [8] designed CuO nanoflower-decorated reduced graphene oxide (CuONF/rGO) nanocomposites for the degradation of Rhodamine B (RhB) under UV irradiation. *Hossain et al.* [14] synthesized CuO and CuO/CdS nanostructures for the photocatalytic degradation of RhB, methyl blue (MB), and methyl orange (MO) under visible light irradiation. Recently, *Akram et al.* [15] reported the synthesis of Ag₂O/CuO nanosheets for the photodegradation of Congo red, RhB, and MO.

The control of nanostructured morphology, particularly in terms of surface area, has the potential to enhance the photocatalytic properties of CuO. Consequently, careful selection of preparation procedures and incorporation of additional metals or metal oxides in CuO-based

^a Department of Chemistry and Biochemistry, North Carolina Central University, Durham, NC 27707. USA

^b Department of Chemistry, Pennsylvania State University, University Park, PA 16802, USA

^{*} Corresponding authors.

E-mail addresses: uriaz@nccu.edu (U. Riaz), fyan@nccu.edu (F. Yan).

 $^{^{1}\,}$ These authors contributed equally.

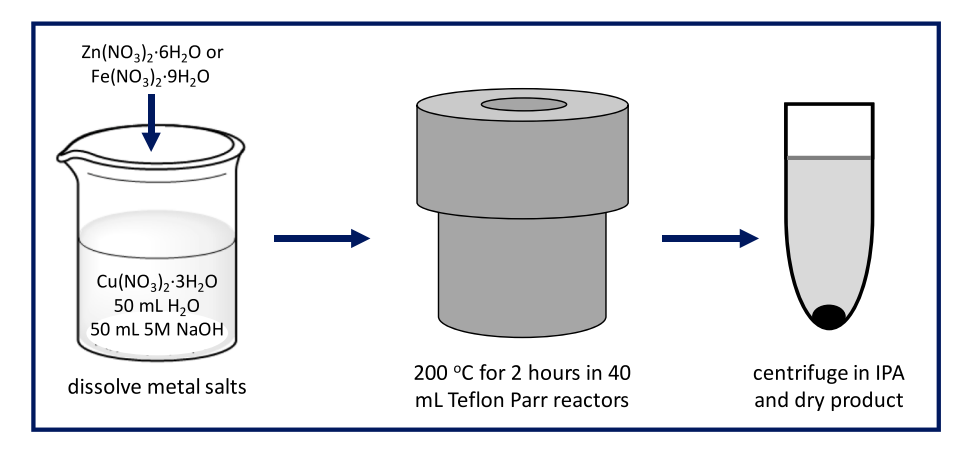


Fig. 1. Schematic illustration of hydrothermal synthesis of Zn/Fe-doped CuO nanosheets.

photocatalysts are crucial steps to achieve the desired properties. These properties encompass maximizing light capture capability, mitigating rapid electron-hole recombination during photocatalysis, and maximizing the generation of electrons/holes under visible light irradiation.

CuO is typically produced as nanostructures with controlled morphology, such as nanorods, nanosheets, and nanodendrites, using various techniques including colloidal methods [16], the sol–gel method [17], and gas phase oxidation [18]. However, these methods often suffer from complexities, time consumption, and/or limited dispersibility of the nanostructures, thereby restricting their broader applicability [19].

In this study, the hydrothermal method was chosen for its cost-effectiveness, ease of handling precursors, and ability to control the structure [20,21]. This method also allows for the formation of various heterostructure morphologies and doping elements. Zhang et al. [22] employed a one-step solvothermal method to prepare CuO-CdS nanowires, aiming to enhance the gas-sensing properties of CuO. *Kakani et al.* [23] utilized a sonication-supported hydrothermal reaction process to design CuO@MnO2 and its nitrogen-doped multiwalled carbon nanotubes (N-MWCNT) composites for evaluating their supercapacitor properties. Meng et al. [24] synthesized nanosheets and CuO/rGO nanocomposites using a one-step hydrothermal method for gas sensing applications. Wang et al. [25] investigated the impact of sulfur doping on the morphology and gas sensing properties of Cu₇S₄-CuO microflowers, which were synthesized via a hydrothermal route.

As discussed earlier, a significant amount of research has been devoted to finding appropriate composites to enhance the photocatalytic properties of CuO. However, doping can also be used to adjust the band gap and electronic properties, such as carrier recombination rates, in CuO. Dopants play a crucial role in influencing the dynamics of electronhole recombination and interfacial charge transfer by acting as traps for both holes and electrons. The degree of metal dispersion on the metal oxide surface is dependent on the doping methods and calcination temperature, resulting in distinct morphological and crystalline properties [26,27]. This approach has gained considerable popularity for enhancing the photocatalytic performance of TiO₂ [28]. In this study, CuO nanosheets were synthesized with Fe and Zn doping to investigate the improved photocatalytic properties. The composition, structure, and morphology of the synthesized nanosheets were confirmed through XRD, TEM, Raman spectroscopy, and XPS characterization techniques. Afterwards, the visible light-assisted photocatalytic activity of the nanosheets was evaluated using malachite green (MG) and MB dyes as representative POPs.

2. Experimental section

2.1. Materials

Malachite green (MG) and methylene blue (MB) were purchased

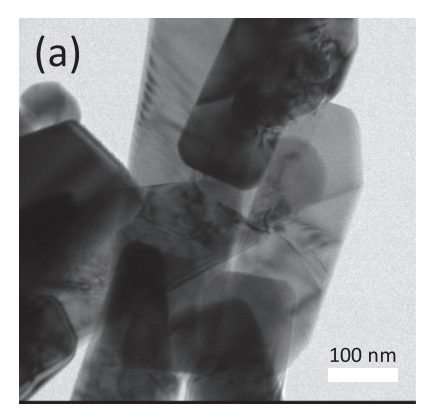
from Fisher Scientific Inc. Cupric nitrate (CN) or $Cu(NO_3)_2 \cdot 3H_2O$ (99–104 %), $Fe(NO_3)_2 \cdot 9H_2O$ (99.95 %), and potassium bromide (spectroscopy quality) were purchased from Sigma-Aldrich, $Zn(NO_3)_2 \cdot 6H_2O$ (99.995 %), NaOH (pellets), isopropyl alcohol (IPA) benzoquinone (BQ), and disodium ethylenediaminetetraacetate acid (Na₂-EDTA) were purchased from VWR.

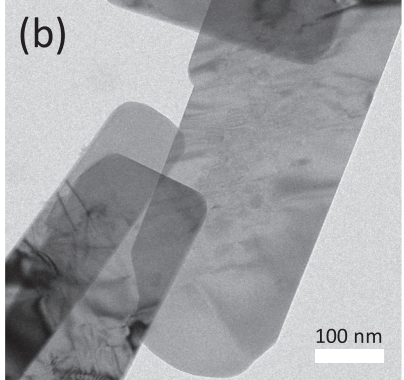
2.2. Synthesis of CuO nanosheets and Zn/Fe-doped CuO nanosheets

As depicted in Fig. 1, the synthesis was conducted according to the procedure outlined by Xiao et al. [29]. $\text{Cu(NO_3)_2} \cdot 3\text{H}_2\text{O}$ (6.04 g for CuO sheets, 5.97 g for doped samples) was dissolved in 50 mL of water. In the case of doped samples containing a target doping level of 1 mol% of either Zn or Fe, $\text{Zn(NO_3)_2} \cdot 6\text{H}_2\text{O}$ (74 mg) or $\text{Fe(NO_3)_2} \cdot 9\text{H}_2\text{O}$ (101 mg) were added to the copper solution. A 5 M NaOH solution (50 mL) was then added to the metal salt solution while stirring. The solution was transferred to four 40 mL Teflon-lined Parr hydrothermal reactors. The reaction was conducted at 200 °C for 2 h. The product was collected and washed by centrifuging in isopropyl alcohol.

2.3. Characterization

Powder X-Ray Diffraction (PXRD) data was collected on a Malvern Panalytical Empyrean diffractometer. The instrument was equipped with a copper source, operated at a voltage of 45 keV and a power of 40 kW. Patterns were obtained utilizing reflection mode and a PIXcel 3D detector. UV-Visible Spectroscopy was collected on a Shimadzu UV-Visible spectrometer equipped with a Harrick praying mantis diffuse reflection accessory. Spectra were referenced to a background of potassium bromide. HORIBA LabRAM HR Evolution Raman microscope with a laser wavelength of 532 nm and a grating with 1800 grooves per mm were used to collect Raman measurements. CuO, Zn-CuO, and Fe-CuO nanosheets were suspended in ethanol and drop cast on a silicon wafer for characterization. A Tecnai G20 20 XTWIN microscope operating at 200 kV was used to collect transmission electron microscopy (TEM) images. X-ray photoelectron spectroscopy (XPS) spectra were collected using a Physical Electronics VersaProbe II instrument equipped with a monochromatic Al K α X-ray source (h ν = 1,486.7 eV) and a concentric hemispherical analyzer. Charge neutralization was performed using both low energy electrons (<5 eV) and argon ions. The binding energy axis was calibrated using sputter cleaned Cu (Cu $2p_{3/2}$ = 932.62 eV, Cu $3p_{3/2} = 75.1$ eV) and Au (Au $4f_{7/2} = 83.96$ eV) foils. Peaks were charge referenced to the CHx band in the carbon 1 s spectra at 285 eV. Measurements were made at a takeoff angle of 45° with respect to the sample surface plane. This resulted in a typical sampling depth of 3-6 nm (95 % of the signal originated from this depth or shallower). Brunauer-Emmett-Teller (BET) surface area measurements were performed using nitrogen adsorption isotherms (Micromeritics ASAP





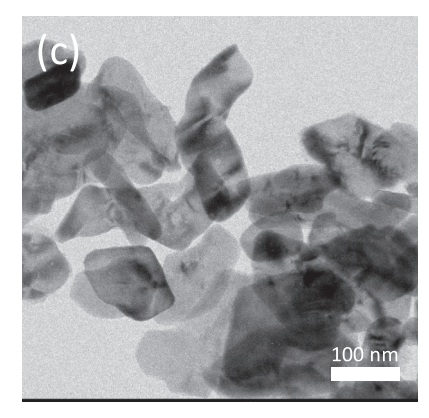


Fig. 2. TEM images of (a) CuO, (b) Zn-CuO, and (c) Fe-CuO nanosheets.

2020). Prior to measurement, the samples were degassed at 90 $^{\circ}$ C for two hours. A 9-point nitrogen adsorption experiment was conducted and fitted by a BET model to obtain the isotherms. The Fukui function was employed to predict sites of reactivity for radicals and electrophilic attacks. Computational calculations were performed using Gaussian 09 software, employing the B3LYP method and a (6311 G) basis set [30].

2.4. Visible light assisted degradation of MB and MG dyes

Visible light irradiation experiments for photocatalytic degradation were conducted using an LS-150-Xe system with a cutoff filter L42 (Newport Corporation). To a stoppered flask with a 100 mL volume containing 50 mL of MB dye with a concentration of 10 ppm, 50 mg of CuO nanosheets were added. The mixture was stirred magnetically for 60 min to achieve absorption-desorption equilibrium and then exposed to visible light irradiation for 270 min. During the treatment, 3 mL aliquots were taken at 30-minute intervals and centrifuged. The spectra were recorded using a VWR UV3100-PC UV—visible spectrophotometer. The same experiment was conducted for the MG solution, but with a 30-minute period of visible light exposure, and the spectra were recorded for aliquots separated at intervals of 5 and 10 min after centrifugation.

2.5. Scavenging test

Scavenging experiments were performed as follows: 50 mg of CuO nanosheets were introduced into a 50 mL MG solution with a concentration of 10 ppm. Solutions containing 5 mM of IPA, CN, and Na2-EDTA, along with a 0.5 mM solution of BQ, were utilized. The suspension underwent sonication for 9 min and subsequent exposure to visible light for 30 min. At designated time intervals, portions of the suspension were withdrawn, and spectral data were recorded using a VWR UV3100-PC UV-visible spectrophotometer.

3. Results and discussion

3.1. Microscopic characterization

Fig. 2(a) displays the TEM image of CuO, illustrating the presence of thin nanosheet structures with lateral dimensions exceeding 100 nm. The darker regions on the particles correspond to thicker stacks of sheets, while the lighter regions indicate single, unstacked nanosheets. Fig. 2(b) shows the TEM image of Zn-CuO, indicating similar nanosheet morphology to the undoped CuO material. Fig. 1(c) shows the TEM image of Fe-CuO, revealing nanosheets with lateral dimensions smaller than the CuO and Zn-CuO samples. The introduced dopants, Zn and Fe, did not greatly influence the morphology of the particles, as all three samples contained nanosheets. The textural properties of these samples were studied using BET analyses, and the surface areas for CuO, Zn-CuO,

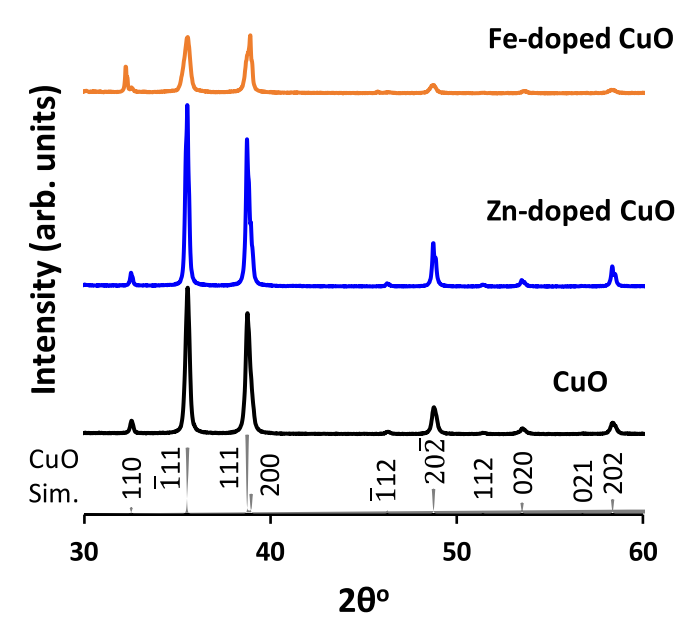


Fig. 3. Experimental PXRD patterns of CuO, Zn-doped CuO, and Zn-doped CuO nanosheets.

and Fe-CuO nanosheets were determined to be $6.8 \text{ m}^2/\text{g}$, $5.5 \text{ m}^2/\text{g}$, and $9.0 \text{ m}^2/\text{g}$, respectively (see Fig. S1, supporting information). These findings indicate that the reported surface areas for the nanosheets fall within a similar range.

3.2. PXRD analysis

The PXRD patterns of the as-prepared CuO nanosheets and the Zn-and Fe-doped CuO nanosheets are shown in Fig. 3. Peaks at $2\theta=35.6^\circ, 38.63^\circ, 48.8^\circ, 54.29^\circ,$ and 58.66° were associated with the Miller planes (\$\overline{1}\$ 11), (200), (\$\overline{2}\$ 02), (020), and (\$\overline{1}\$ 13), respectively, and are consistent with the monoclinic (tenorite) phase of CuO. The PXRD patterns closely corresponded to the simulated patterns of CuO [31]. The diffraction pattern also confirmed high crystalline phase purity, as peaks that would have correlated to Cu₂O and/or Cu(OH)₂ were not observed. The PXRD patterns for the Zn-CuO and Fe-CuO nanosheets matched closely to that of pristine CuO with no noticeable shifts in peak position. Additionally, there were no observable peaks due to either of the transition metals or their oxides (Fe, Zn), indicating no significant crystalline impurities.

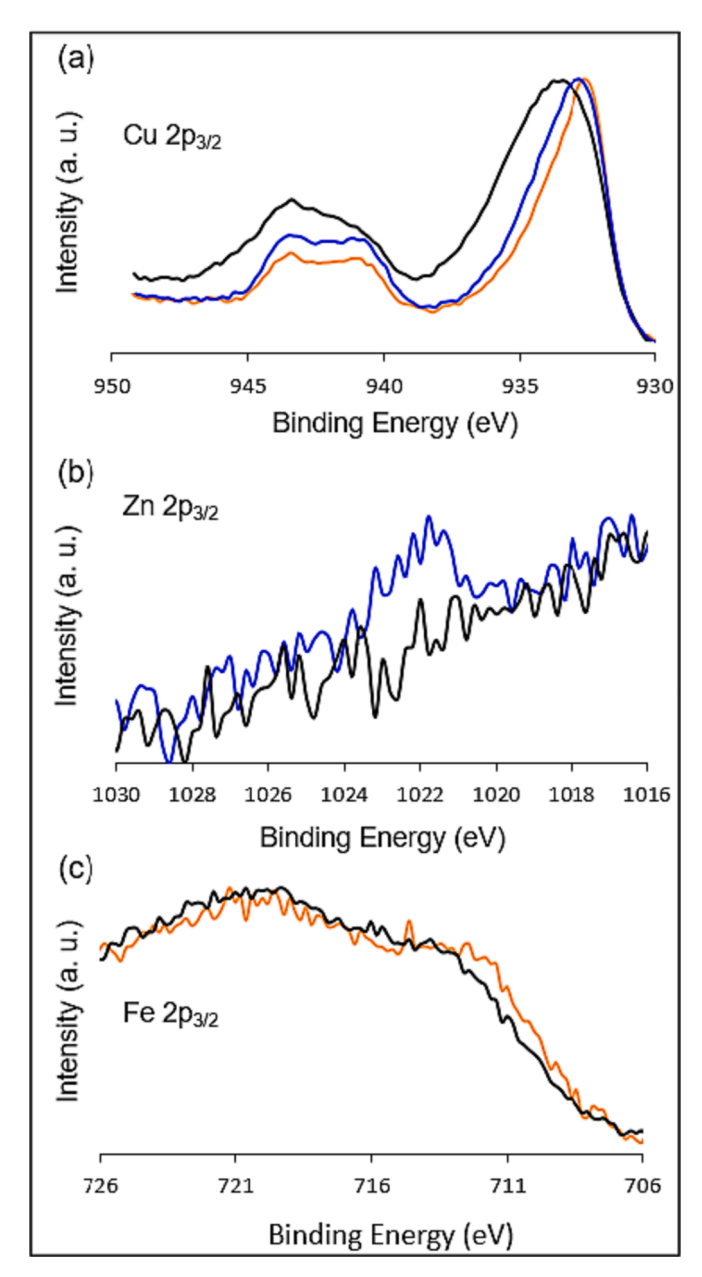


Fig. 4. High-resolution XPS spectra for the (a) Cu $2p_{3/2}$, (b) Zn $2p_{3/2}$, and (c) Fe $2p_{3/2}$ regions. All black spectra correspond to the pristine CuO, blue correspond to Zn-doped CuO, and orange correspond to Fe-doped CuO. (For interpretation of the references to colour in this figure legend, the reader is referred to the web version of this article.)

3.3. X-ray photoelectron spectroscopy

Fig. 4(a) shows high-resolution XPS spectra for the Cu $2p_{3/2}$, Zn $2p_{3/2}$, and Fe $2p_{3/2}$ regions of the pristine and doped CuO samples. All spectra in each region were normalized to one another to better evaluate the presence of the Zn and Fe dopants. In the Cu $2p_{3/2}$ region of the pristine and doped samples, the shifting of the CuO peak at 933.6 eV is attributed to charging and not effects from Zn or Fe doping. The shake-up peaks ~ 10 eV higher than the Cu $2p_{3/2}$ peak designate the presence of Cu²⁺ in CuO [32], indicating that the surface of the material contains largely CuOAs the Zn and Fe doping levels were low, the resulting XPS signal in each region was also low, so we included the high-resolution XPS spectra in the Zn $2p_{3/2}$ and Fe $2p_{3/2}$ regions for the pristine CuO sample to confirm that Zn and Fe had been incorporated in Zn-CuO and Fe-CuO, respectively. Fig. 4(b) shows the Zn $2p_{3/2}$ region for both the

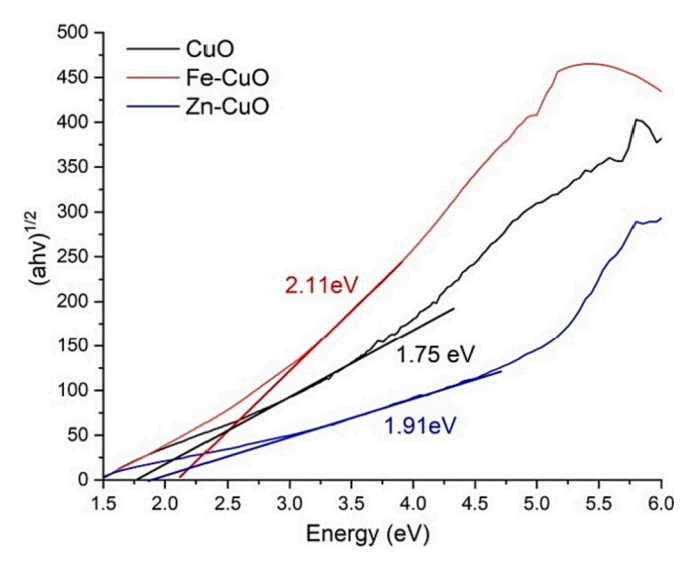


Fig. 5. Direct band gap calculation utilizing the Kubelka-Munk function for CuO, Fe-CuO, and Zn-CuO nanosheets.

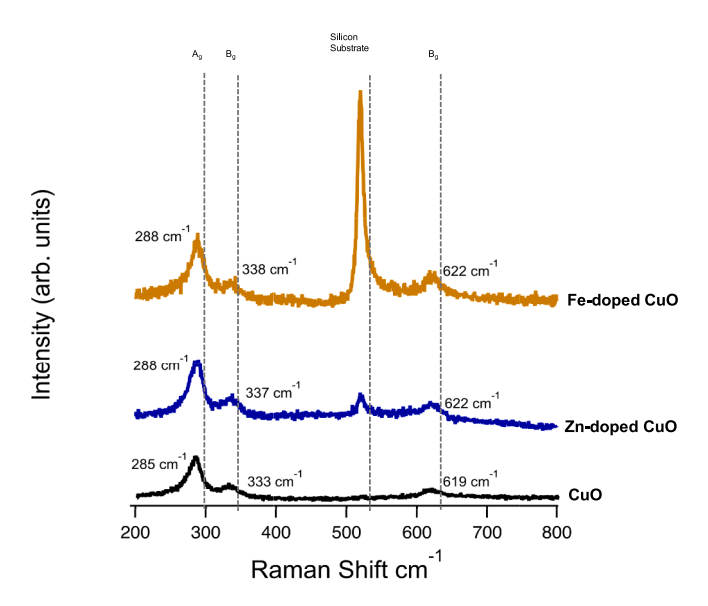


Fig. 6. Raman spectra of CuO, Zn-CuO, and Fe-CuO nanosheets.

pristine CuO and the Zn-doped CuO. The peak in the Zn-doped sample at 1021.8 eV, which is absent in pristine CuO, indicates its presence at low levels in the Zn-doped sample [33,34]. The Fe $2p_{3/2}$ region in Fig. 4(c) overlaps with a Cu Auger peak, which makes unambiguous identification challenging. However, the Fe-CuO sample contains a broad and low-intensity shoulder around 711 eV, rather than a sharper peak due to the low doping concentration [33]. The pristine CuO sample does not contain this shoulder, which is consistent with the presence of a small amount of Fe in the doped sample.

3.4. UV-Vis diffusive reflectance spectroscopy

Ultraviolet—visible diffuse reflectance spectroscopy was used to examine the light absorption properties of pristine CuO and CuO nanosheets doped with Zn and Fe. The optical band gaps were calculated by analyzing Kubelka-Munk function plots. From the most linear regions in Fig. 5, the extrapolated band gap values were determined as follows: 2.11 eV for CuO nanosheets, 1.91 eV for Zn-doped CuO nanosheets, and 1.75 eV for Fe-doped CuO nanosheets. These slight reductions in band

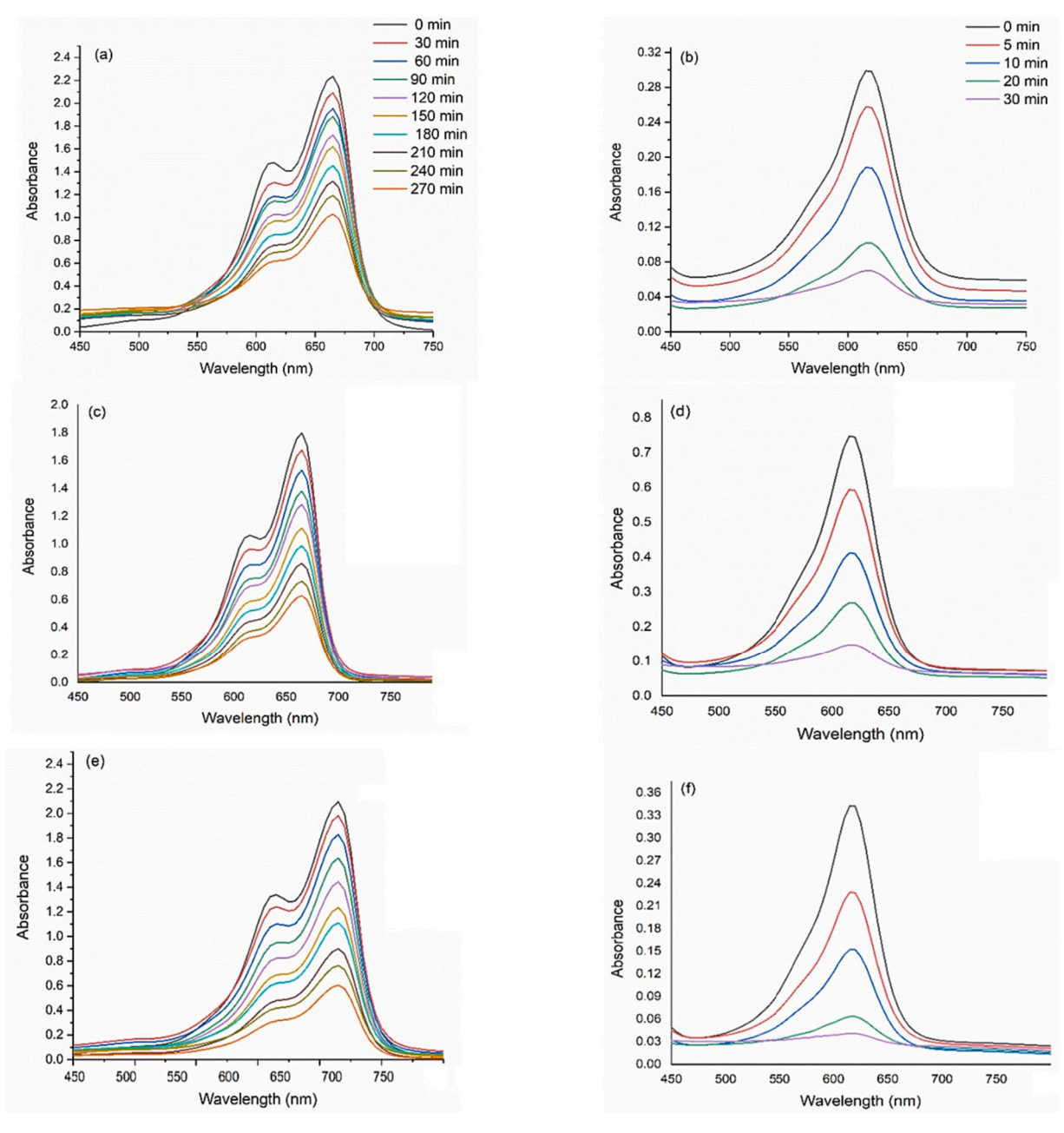


Fig. 7. UV-visible spectra of dye degradation using (a) CuO nanosheets in MB dye, (b) CuO nanosheets in MG dye, (c) Zn-CuO nanosheets in MB dye, (d) Zn-CuO nanosheets in MG dye, (e) Fe-CuO nanosheets in MB dye, and (f) Fe-CuO nanosheets in MG dye.

gap may be attributed to the introduction of new d-band energy levels at the bottom of the conduction band, similar to observations in ${\rm TiO_2}$ [35]. However, considering the uncertainties in estimating the slope of the linear regions, the band gaps of all three samples remain relatively similar, indicating that the dopants have a minimal impact on the optical properties. Nonetheless, all three samples fall within the 1–3 eV range, making them active photocatalysts under visible light irradiation.

3.5. Raman spectroscopy

Raman spectra of CuO nanosheets and CuO nanosheets doped with Zn and Fe are shown in Fig. 6. All the samples show three Raman peaks around 286, 333, and 617 ${\rm cm}^{-1}$, which are associated with the $A_g,\,B_{g1},$ and B_{g2} modes of the monoclinic CuO nanosheets [31]. The slight shifting of peaks in the Zn (blue) and Fe (orange) doped samples as compared to pristine CuO (black) is attributed to compressive stress

arising from the dopant elements [36], thus affirming their incorporation into the CuO crystal structure [37].

3.6. Visible light induced photodegradation of MB and MG dyes

The UV–visible spectra of MB and MG dyes (at a concentration of 10 ppm) demonstrate degradation in the presence of CuO photocatalysts (at a dosage of 50 mg), as depicted in Fig. 7. The dye degradation experiments were carried out over 270 min for MB dye and over 30 min for MG dye, which represent times required for maximum degradation to occur. There was a consistent decrease in the absorbance values for the MB and MG dyes in the presence of CuO photocatalysts, as shown in Fig. 7(a and b). In the presence of Zn-CuO nanosheets, the dyes were found to show a higher rate of degradation with time as compared to pristine CuO nanosheets, Fig. 7(c and d). The highest degradation rate was observed in the presence of Fe-CuO nanosheets, Fig. 7(e and f).

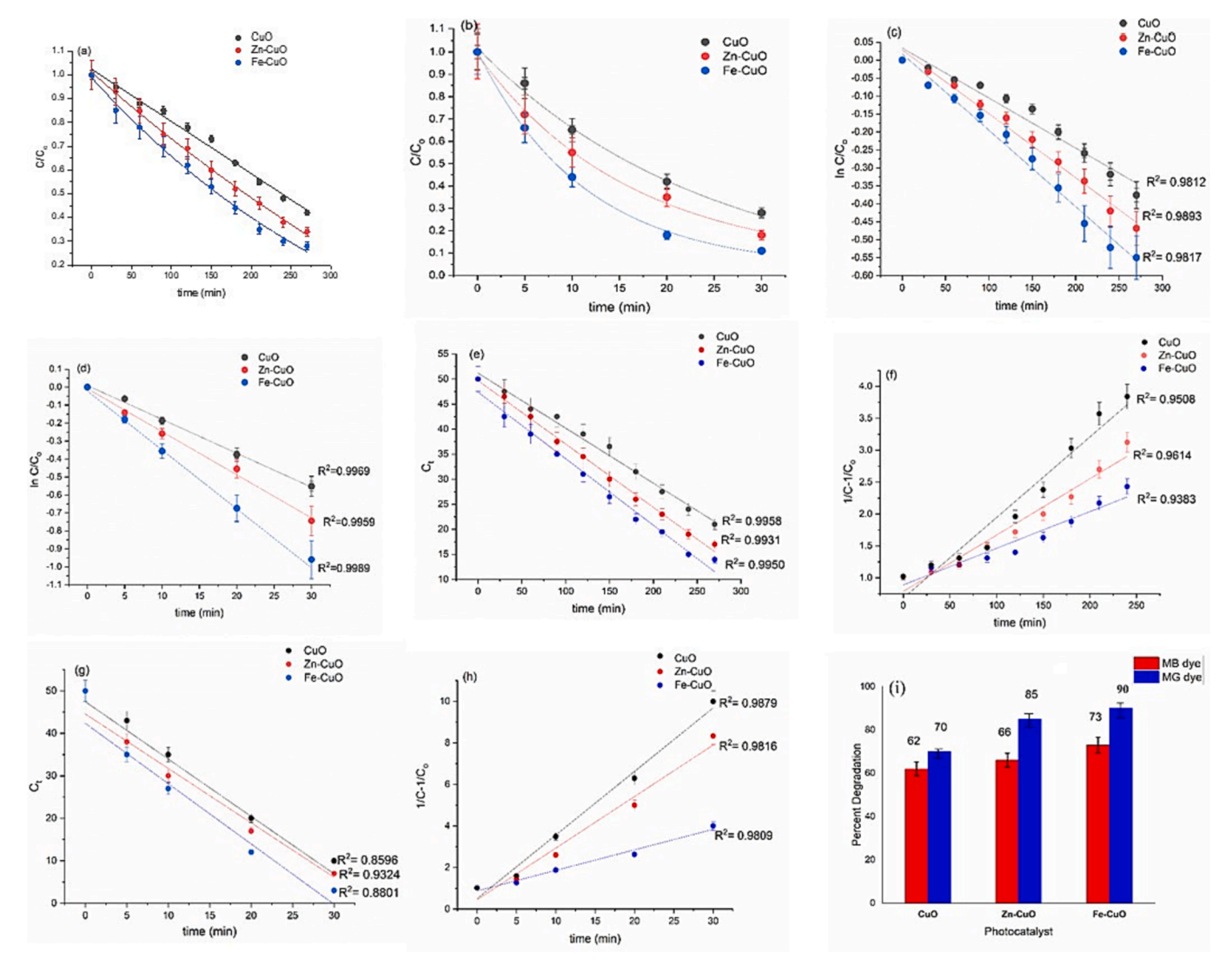


Fig. 8. (a) C/C_o plot for MB dye, (b) C/C_o plot for MG dye, (c) $\ln C/C_o$ plot for MB dye, (d) $\ln C/C_o$ plot for MG dye, and (e) zero order plot for MB dye, (f) pseudo second order plot for MB dye, (g) zero order plot for MG dye, (h) pseudo second order plot for MG dye, (i) the degradation efficiency graph showing percent degradation of MB and MG dyes in the presence of CuO, Zn-CuO, and Fe-CuO nanosheets.

Fig. 8(a – d) illustrate the zero-order, first-order, and pseudo-secondorder plots for MB and MG degradation. It is evident that MB degradation conforms to zero-order kinetics (Fig. 8e), whereas MG degradation adheres to a first-order kinetics model (Fig. 8d). The pristine CuO nanosheets revealed 62 % degradation for MB dye and 70 % degradation for MG dye, respectively, Fig. 8(e). However, in the presence of Zn-CuO, the MB dye revealed 66 % degradation, while MG dye showed almost 85 % degradation within 270 min and 30 min, respectively. The rate constant (k) values for the degradation of MB dye were determined to be $1.2 \times 10^{-2} \text{ min}^{-1}$, $1.8 \times 10^{-2} \text{ min}^{-1}$, and $2.1 \times 10^{-2} \text{ min}^{-1}$ for CuO, Zn-CuO, and Fe-CuO, respectively. Similarly, the values for the degradation of MG dye was determined to be $1.8 \times 10^{-2} \,\mathrm{min}^{-1}$, $2.4 \times 10^{-2} \,\mathrm{min}^{-1}$ and 3.2×10⁻² min⁻¹ for CuO, Zn-CuO, and Fe-CuO nanosheet photocatalysts, respectively. Table 1 demonstrates that the CuO nanosheets synthesized in this study exhibit superior degradation capabilities compared to those reported by others.

The rate constants for the degradation of MB dye and MG dye using Zn-CuO and Fe-CuO nanosheets are much higher than the reported rate constants for visible-light photocatalysts, such as TiO₂, ZnO, and BiVO₄. which range from $0.4\times10^{-2}-0.8~\text{min}^{-1}$ for MB dye [38] and $0.5\times10^{-2}~\text{min}^{-1}$ to $1.7\times10^{-2}~\text{min}^{-1}$ for MG dye [39]. This suggests that Zn-CuO and Fe-CuO nanosheets are more effective photocatalysts for the

degradation of MB dye and MG dye under visible light irradiation than TiO_2 , ZnO_3 , and $BiVO_4$ photocatalysts.

3.7. Scavenging studies and recyclability tests

Fig. 9(a) shows the results of the photocatalytic degradation of MG dye by Fe-doped CuO nanosheets with various scavengers: IPA, BQ, Na₂-EDTA, and CN. These scavengers target hydroxyl radicals (${}^{\bullet}$ OH), superoxide radicals (${}^{\bullet}$ O ${}^{-}$), holes (h ${}^{+}$), and electrons (e ${}^{-}$), respectively [43]. The degradation efficiency of photocatalysts refers to the percentage of dyes that were removed or degraded from the solution. The Fe-CuO nanosheets exhibited an approximately 90 % degradation efficiency in the absence of the scavenger. The inclusion of IPA, BQ, Na₂-EDTA, and CN led to a decrease in the degradation efficiency, yielding percentages of 28.5 %, 84 %, 72 %, and 60 % respectively. This confirms the dominance of ${}^{\bullet}$ OH radicals in degrading the MG dye, aligning with findings for the MB dye [43]. Recycleability tests, as indicated in Fig. 9 (b), demonstrated that the photocatalyst remained effective for a single cycle only.

Table 1
Comparative analysis of dye degradation using CuO nanosheets.

Catalyst	Dye Concentration (M, or ppm)	Amount of photocatalyst	% Degradation	Time (min)	References
CuO nanosheets	MB (10^{-4} M)	10 mg	97	180	[40]
	Eosin Y (10 ⁻⁴ M)	10 mg	99.1	40	[40]
CuO nanosheets	RhB (10 ppm)	20 mg	65	160	[41]
	MO (4 ppm)	20 mg	49.3	160	[41]
CuO nanosheets	MO (20 ppm)	_	70	120	[42]
Ag-decorated CuO nanosheets	MO (20 ppm)	-	99	120	[42]
CuO nanosheets	RhB (3×10 ⁻⁵ M)	200 mg	15	300	[37]
	MB $(3\times10^{-5} \text{ M})$	200 mg	90	300	[37]
CuO nanosheets	MB (10 ppm)	50 mg	62	270	This work
	MG (10 ppm)	50 mg	70	30	This work
Zn-CuO nanosheets	MB (10 ppm)	50 mg	66	270	This work
	MG (10 ppm)	50 mg	85	30	This work
Fe-CuO nanosheets	MB (10 ppm)	50 mg	66	270	This work
	MG (10 ppm)	50 mg	90	30	This work

Fig. 9(a) shows the results of the photocatalytic degradation of MG dye by Fe-doped CuO nanosheets with various scavengers: IPA, BQ, Na₂-EDTA, and CN. These scavengers target hydroxyl radicals ('OH), superoxide radicals ('O₂⁻), holes (h⁺), and electrons (e⁻), respectively [43]. The degradation efficiency of photocatalysts refers to the percentage of dyes that were removed or degraded from the solution. The Fe-CuO nanosheets exhibited an approximately 90% degradation efficiency in the absence of the scavenger. The inclusion of IPA, BQ, Na₂-EDTA, and CN led to a decrease in the degradation efficiency, yielding percentages of 28.5%, 84%, 72%, and 60% respectively. This confirms the dominance of •OH radicals in degrading the MG dye, aligning with findings for the MB dye [43]. Recycleability tests, as indicated in Fig. 9(b), demonstrated that the photocatalyst remained effective for a single cycle only.

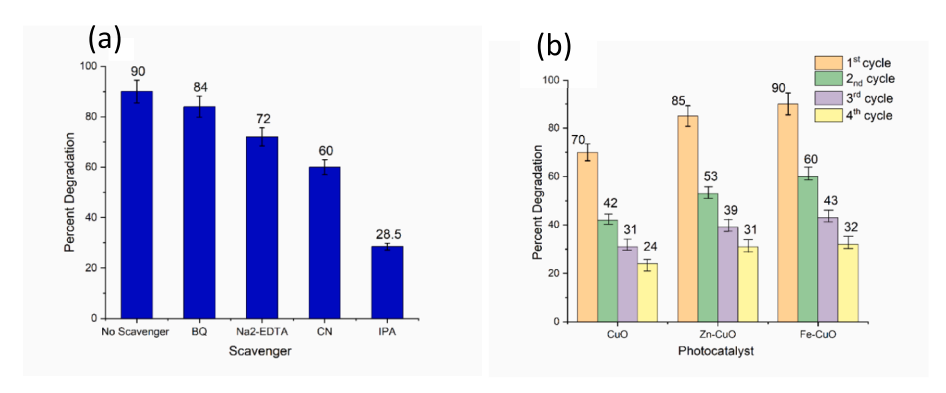
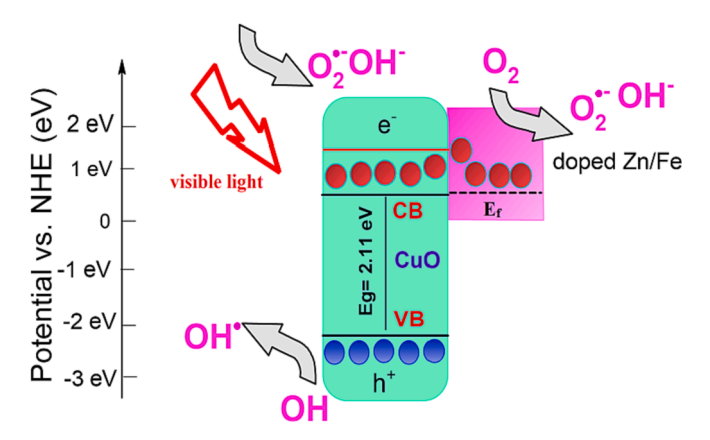


Fig. 9. (a) Effect of Fe-CuO nanosheets on the percent degradation of the MG dye in the presence of different scavengers; and (b) Recyclability tests of CuO, Zn-CuO and Fe-CuO photocatalysts.



Scheme 1. Proposed mechanism of photocatalytic degradation of dyes using Zn/Fe-doped CuO nanosheets.

${\it 3.8. Proposed mechanism for photocatalytic dye degradation using CuO} \\ {\it nanosheets}$

Earlier investigations on Co-doped CuO nanosheets have shown that reducing the band gap can enhance absorbance in the visible region, resulting in increased excited carriers and improved catalytic activity [31,32,33]. Moreover, the presence of dopant atoms induce favorable surface binding energies by introducing local strain effects [13,34]. Upon exposure to visible light, the photocatalyst absorbs photons, leading to the excitation of electrons from the valence band (VB) to the conduction band (CB), as shown in Scheme 1. CuO is composed of Cu-3d and O-2p shells occupied CB and VB edges, resulting in a lower bandgap. This configuration maximizes •OH generation and enhances visible light absorption. The CuO photocatalyst, with a 2.11 eV bandgap, possesses CB and VB potentials of 0.45 V and 2.56 V, respectively, which are sufficient for the release of •OH and •O₂ radicals required for photodegradation under visible light. When photons are absorbed by the photocatalyst, some electrons transition from the VB to the CB, thereby generating electrons and holes in the CB and VB bands, respectively. These electrons and holes can produce •OH free radicals, which are

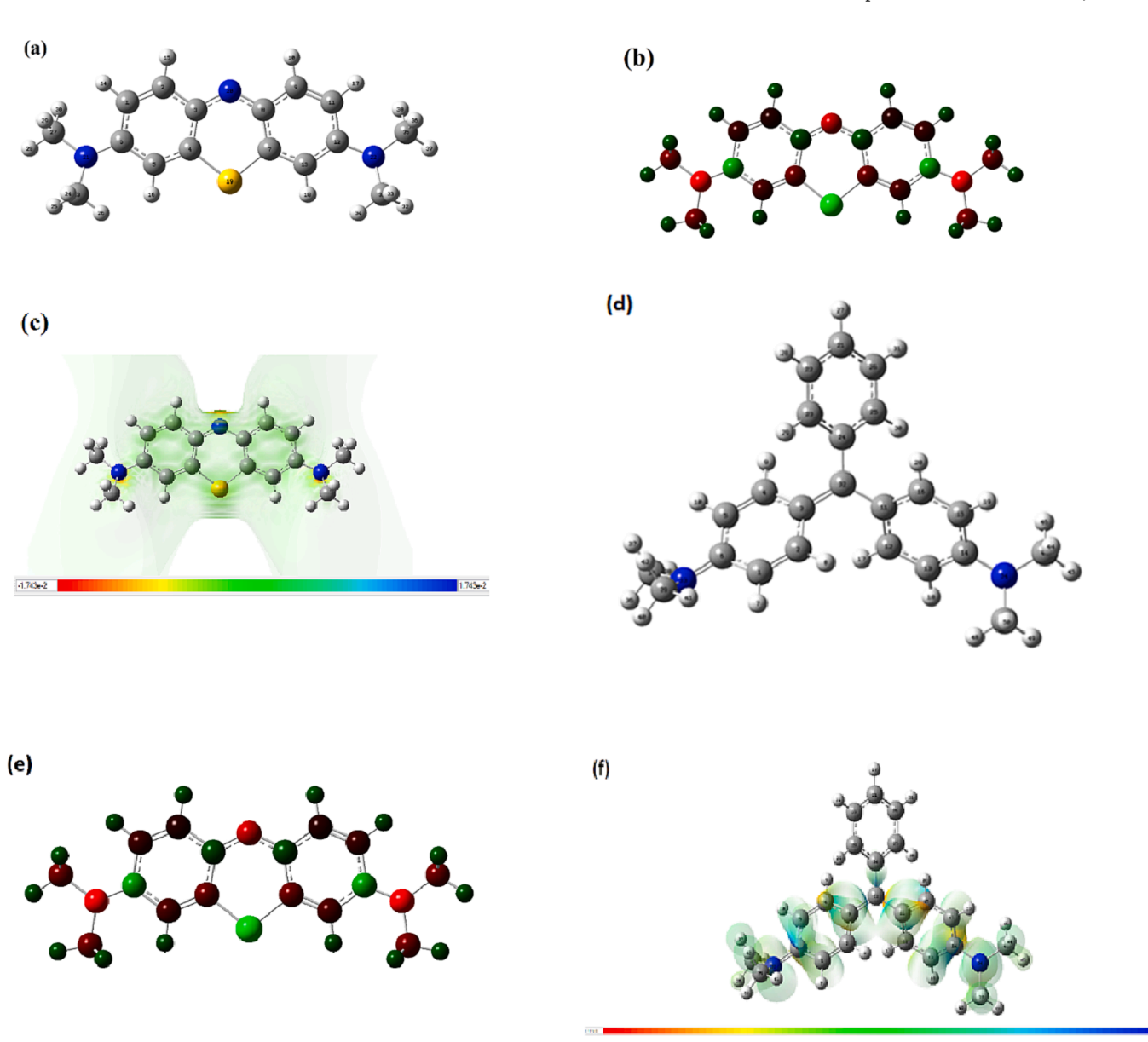


Fig. 10. (a) Optimized geometry of MB dye, (b) Muliken charge distribution in MB dye, (c) electrostatic surface potential of MB dye, (d) Optimized geometry of MG dye, (e) Muliken charge distribution in MG dye, and (f) electrostatic surface potential of MG dye.

potent nonselective oxidizing agents for degrading organic pollutants. Additionally, the presence of metal dopants on the surface improves photocatalytic activity by trapping charge carriers, effectively inhibiting recombination through charge carrier separation on various sites. Moreover, these dopants interact with the dye, creating pathways for interfacial charge transfer, resulting in faster degradation.

It is hypothesized that the photocatalytic degradation of dyes in the presence of pristine and/or transition metal-doped CuO nanosheets proceeds through the following reactions:

$$CuO + h\nu \text{ (visible light)} \rightarrow h_{VB}^{+} + e_{CB}$$
 (1)

$$H_2O \rightarrow H^+ + OH^- \tag{2}$$

$$\cdot OH^{-} + h_{VB}^{+} \rightarrow \cdot O \tag{3}$$

$$e_{CB}^{-} + O_2 \rightarrow O_2^{\bullet -} \tag{4}$$

$$O_2^{\bullet -} + H^+ \rightarrow {}^{\bullet}OOH$$
 (5)

$$2^{\bullet}OOH \rightarrow H_2O_2 + O_2$$
 (6)

$$H_2O_2 + \text{visible light} \rightarrow {}^{\bullet}OH$$
 (7)

$$Dye + {}^{\bullet}OH \rightarrow Dye \text{ degradation products}$$
 (8)

3.9. Fukui index values

DFT calculations were used to compute the Fukui index, which predicts the radical attack (f°) and electrophilic attack (f⁻) on the MB and MG dye (see Tables S1 and S2, supporting information). For the MG dye, with regard to electrophilic attack, the Fukui index values emphasize the vulnerability of carbon atoms 4C, 5C, 7C, 13C, 23C, and 27C, in addition to nitrogen atoms at positions 21 N and 22 N, as well as sulfur (19S). Conversely, notable sites susceptible to free radical attack were pinpointed, particularly at carbon atoms 3C, 5C, 12C, and 19S, displaying significantly heightened Fukui index values. In the case of the MG dye, the carbon atoms prone to radical attack were recognized as 2C, 4C, 5C, 6C, 16C, and 21C. Conversely, sites susceptible to electrophilic attack were detected at 6C, 14C, and 32C. Furthermore, the nitrogen atoms exhibited a propensity for electrophilic attack. The optimized DFT geometries for MB and MG dves are illustrated in Fig. 10(a and d), respectively. Analysis of the charge distribution in Fig. 10(b and e) demonstrates significant charge accumulation around the nitrogen atoms in both the MB and MG dye structures. Examining the electrostatic surface potential (ESP) in Fig. 10(c and f) reveals the molecules' neutral nature for both MB and MG dyes.

3.10. Limitations of this study

This study has certain limitations that deserve attention. Firstly, quantifying the low doping level of approximately 1 mol% for Zn or Fe through SEM/EDX analysis presents a significant challenge, emphasizing the need for higher doping levels. Secondly, our current setup lacks real-time total organic carbon (TOC) detection, which has led us to rely on monitoring absorbance intensity to assess degradation efficiency. To address this limitation, we plan to incorporate liquid chromatography-mass spectrometry (LC-MS) in our future research. Furthermore, the observed decrease in photocatalytic degradation efficiency over subsequent cycles suggests that achieving higher levels of doping in CuO nanosheets may be necessary for sustained effectiveness, emphasizing the importance of further optimization in future investigations. Lastly, it's essential to evaluate the treated solution's biocompatibility in the context of industrial pollutants [44], while considering the stability issue of the CuO nanosheets.

4. Conclusion

In this study, CuO nanosheets, as well as Zn-doped CuO and Fe-doped CuO nanosheets, were synthesized and examined for their photocatalytic performance in the degradation of MG and MB when exposed to visible light. The confirmation of Zn and Fe doping was achieved through UV-DRS, XPS, and Raman analysis. The doped nanosheets exhibited enhanced photocatalytic activity compared to undoped CuO, with Zn- and Fe-doped CuO nanosheets demonstrating higher efficiency in degrading the dyes. Specifically, within 270 min, Zn and Fe-doped CuO nanosheets degraded 66 % and 73 % of MB dye, respectively, while CuO nanosheets alone achieved a degradation rate of 62 %. Additionally, within 30 min, Zn and Fe-doped CuO nanosheets degraded 85 % and 90 % of MG dye, respectively, compared to 76 % degradation achieved by CuO nanosheets alone. In the optimized geometry of both MB and MG dyes, DFT calculations unveil significant charge accumulation surrounding N atoms. Electrostatic potential analysis corroborates the neutrality of the molecules. Furthermore, the resulting Fukui index underscores the vulnerability of specific carbon, nitrogen, and sulfur sites to both electrophilic and radical attacks. The enhanced photocatalytic activity of Fe-CuO nanosheets was attributed to its slightly lower band gap. These findings have significant implications for the development of effective photocatalysts for the remediation of other POPs under visible light. Furthermore, the study provides a motivation for future research in this area, which could lead to the development of novel, highly efficient photocatalysts for environmental remediation applications.

Author Contributions

F.Y. and U.R. designed this study. T.S., R.K., K.T., S.A., B.C. and A. S. performed the experiments. U.R. conducted the DFT calculations. T.S., R.K., and K.T. analyzed the data and drafted the manuscript. F.Y., U.R., and R.S. revised the manuscript. All authors accepted to submit for publication.

CRediT authorship contribution statement

Tank R. Seling: Methodology, Investigation, Data curation. Rowan R. Katzbaer: Methodology, Investigation, Data curation. Katherine L. Thompson: Writing – original draft, Methodology, Investigation, Data curation. Sophia E. Aksoy: Investigation. Basant Chitara: Methodology, Investigation. Amit K. Shringi: Investigation, Data curation. Raymond E. Schaak: Writing – review & editing, Supervision. Ufana Riaz: Writing – review & editing, Writing – original draft, Methodology, Formal analysis, Conceptualization. Fei Yan: Writing – review & editing, Supervision, Funding acquisition.

Declaration of Competing Interest

The authors declare that they have no known competing financial interests or personal relationships that could have appeared to influence the work reported in this paper.

Data availability

Data will be made available on request.

Acknowledgements

The authors T.S., B.C., U.R., and F.Y. acknowledge the financial support of the U.S. National Science Foundation (Award #2122044) for this project. This research was partially sponsored by the Army Research Office and was accomplished under Grant W911NF2210109. The views and conclusions contained in this document are those of the authors and should not be interpreted as representing the official policies, either expressed or implied, of the Army Research Office or the U.S. Government. The U.S. Government is authorized to reproduce and distribute

reprints for Government purposes notwithstanding any copyright notation herein. R.K., K.T., S.A., and R.S. thank Penn State University for funding. TEM, XRD, XPS, BET, and UV-Vis data were acquired at the Materials Characterization Lab of the Penn State Materials Research Institute The authors thank Gino Tambourine for acquiring BET data and Obed Keelson and Abiodun Folarin for their contributions in conducting initial MS measurements to identify intermediate products.

Appendix A. Supplementary data

Supplementary data to this article can be found online at https://doi.org/10.1016/j.jphotochem.2023.115356.

References

- [1] M. Sabri, A. Habibi-Yangjeh, S.R. Pouran, C. Wang, Titania-activated persulfate for environmental remediation: the-state-of-the-art, Catal. Rev. 65 (2023) 118–173, https://doi.org/10.1080/01614940.2021.1996776.
- [2] S. Feizpoor, S.R. Pouran, A. Habibi-Yangjeh, Recent progress on photocatalytic evolution of hydrogen gas over TiO₂-x-based emerging nanostructures, Mater. Sci. Semicond. Process. 162 (2023), 107444, https://doi.org/10.1016/j. mssp.2023.107444.
- [3] U. Riaz, S.M. Ashraf, V. Budhiraja, S. Aleem, J. Kashyap, Comparative studies of the photocatalytic and microwave–assisted degradation of alizarin red using ZnO/ poly (1- naphthylamine) nanohybrids, J. Mol. Liq. 216 (2016) 259–267, https:// doi.org/10.1016/j.molliq.2016.01.018.
- [4] U. Riaz, S.M. Ashraf, J. Kashyap, Enhancement of photocatalytic properties of transitional metal oxides using conducting polymers: A mini review, Mater. Res. Bull. 71 (2015) 75–90, https://doi.org/10.1016/j.materresbull.2015.06.035.
- [5] A. Akhundi, A.Z. Moshfegh, A. Habibi-Yangjeh, M. Sillanpää, Simultaneous dualfunctional photocatalysis by g-C₃N₄-based nanostructures, ACS EST Engg. 2 (2022) 564, https://doi.org/10.1021/acsestengg.1c00346.
- [6] M.R. Rajeshwari, S. Kokilavani, S.S. Khan, Recent developments in architecturing the g-C3N4 based nanostructured photocatalysts: Synthesis, modifications and applications in water treatment, Chemosphere 291 (2022), 132735, https://doi. org/10.1016/j.chemosphere.2021.132735.
- [7] M. Nazim, A.A.P. Khan, A.M. Asiri, J.H. Kim, Exploring rapid photocatalytic degradation of organic pollutants with porous CuO nanosheets: Synthesis, dye removal, and kinetic studies at room temperature, ACS Omega 6 (2021) 2601–2612, https://doi.org/10.1021/acsomega.0c04747.
- [8] S. Liu, J. Tian, L. Wang, Y. Luo, X. Sun, One-pot synthesis of CuO nanoflower-decorated reduced graphene oxide and its application to photocatalytic degradation of dyes, *Catal*, Sci. Technol. 2 (2012) 339–344, https://doi.org/10.1039/CICY00374G.
- [9] L. Wang, X. Zhang, H. Gao, J. Hu, J. Mao, C. Liang, P. Zhang, G. Shao, 3D CuO network supported TiO2 nanosheets with applications for energy storage and water splitting, Sci. Adv. Mater. 8 (2016) 1256–1262, https://doi.org/10.1166/sam.2016.2714
- [10] N.M.E. Shafai, R. Ji, M. Abdelfatah, M.A. Hamada, A.W. Kandeal, I.M. El-Mehasse, A.E. Shaer, M. An, M.S. Ramadan, S.W. Sharshir, W. Ismail, Investigation of a novel (GO@CuO.γ-Al2O3) hybrid nanocomposite for solar energy applications, J. Alloys. Cmpds. 856 (2021), 157463, https://doi.org/10.1016/j.jallcom.2020.157463.
- [11] A. Ghosh, M. Miah, A. Bera, S.K. Saha, B. Ghosh, Synthesis of freestanding 2D CuO nanosheets at room temperature through a simple surfactant free co-precipitation process and its application as electrode material in supercapacitors, J. Alloys. Cmpds. 862 (2021), 158549, https://doi.org/10.1016/j.jallcom.2020.158549.
- [12] S.D. Jagadale, A.M. Teli, S.V. Kalake, A.D. Sawant, A.A. Yadav, P.S. Patil, Functionalized crown ether assisted morphological tuning of CuO nanosheets for electrochemical supercapacitors, J. Electroanal. Chem. 816 (2018) 99–106, https://doi.org/10.1016/j.jelechem.2018.01.059.
- [13] A.M.E. Sayed, M. Shaban, Structural, optical and photocatalytic properties of Fe and (Co, Fe) co-doped copper oxide spin coated films, Spectrochim Acta. A Mol. Biomol. Spectr. 149 (2015) 638–646, https://doi.org/10.1016/j.saa.2015.05.010.
- [14] S.S. Hossain, M. Tarek, T.D. Munusamy, K.M.R. Karim, S.M. Roopan, S.M. Sarkar, C.K. Cheng, M.M.R. Khan, Facile synthesis of CuO/CdS heterostructure photocatalyst for the effective degradation of dye under visible light, Environ. Res. 188 (2020), 109803, https://doi.org/10.1016/j.envres.2020.109803.
- [15] N. Akram, J. Guo, Y. Guo, Y. Kou, H. Suleman, J. Wang, Enhanced synergistic catalysis of novel Ag₂O/CuO nanosheets under visible light illumination for the photodecomposition of three dyes, J. Environ. Chem. Eng. 9 (2021), 104824, https://doi.org/10.1016/j.jece.2020.104824.
- [16] S. Anandam, G.J. Lee, J.J. Wu, Sonochemical synthesis of CuO nanostructures with different morphology, Ultrason. Sonochem. 19 (2012) 682–686, https://doi.org/ 10.1016/j.ultsonch.2011.08.009.
- [17] V. Dhanasekaran, N. Soundaram, S. Kim, R. Chandramohan, S. Mantha, S. Saravanakumar, T. Mahalingam, Optical, electrical and microstructural studies of monoclinic CuO nanostructures synthesized by a sol–gel route, New J. Chem. 38 (2014) 2327–2333, https://doi.org/10.1039/C4NJ00084F.
- [18] Q. Zhang, K. Zhang, D. Xu, G. Yang, H. Huang, F. Nie, C. Liu, S. Yang, CuO nanostructures: Synthesis, characterization, growth mechanisms, fundamental properties, and applications, Prog. Mater. Sci. 60 (2014) 208–337, https://doi.org/ 10.1016/j.pmatsci.2013.09.003.

- [19] M.V. Umar, S.H. Kim, Y.-B. Hahn, Low-temperature synthesis of flower-shaped CuO nanostructures by solution process: Formation mechanism and structural properties, J. Phys. Chem. C 112 (2008) 5729–5735, https://doi.org/10.1021/ iv71.0358i
- [20] M. Outokesh, M. Hosseinpour, S.J. Ahmadi, T. Mousavand, S. Sadjadi, W. Soltanian, Hydrothermal synthesis of CuO nanoparticles: Study on effects of operational conditions on yield, purity, and size of the nanoparticles, Ind. Eng. Chem. Res. 50 (2011) 3540–3554, https://doi.org/10.1021/ie1017089.
- [21] S. Sonia, S. Poongodi, P.S. Kumar, D. Mangalaraj, N. Ponpandian, C. Viswanathan, Hydro-thermal synthesis of highly stable CuO nanostructures for efficient photocatalytic degradation of organic dyes, Mater. Sci. Semicond. Proc. 30 (2015) 585–591, https://doi.org/10.1016/j.mssp.2014.10.012.
- [22] N. Zhang, X. Ma, Y. Yin, Y. Chen, C. Li, J. Yin, S. Ruan, Synthesis of CuO-CdS composite nanowires and their ultrasensitive ethanol sensing properties, Inorg. Chem. Front. 6 (2019) 238–247, https://doi.org/10.1039/C8Q100951A.
- [23] V. Kakani, S. Ramesh, H.M. Yadav, C. Bathula, P.K. Basivi, R.R. Palem, H.S. Kim, V. R. Pasupuletti, H. Lee, H. Kim, Hydrothermal synthesis of CuO@MnO2 on nitrogen-doped multiwalled carbon nanotube composite electrodes for supercapacitor applications, Sci. Rep. 12 (2022) 12951, https://doi.org/10.1038/s41598-022-16863-3.
- [24] F. Meng, Z. Yang, Z. Yuan, H. Zhang, H. Zhu, Hydrothermal synthesis of CuO/rGO nanosheets for enhanced gas sensing properties of ethanol, Ceram. Int. 49 (2023) 5595–5603, https://doi.org/10.1016/j.ceramint.2022.10.174.
- [25] N. Wang, R. Jin, Y. Zhou, L. Zhao, T. Wang, L. Zhao, F. Liu, X. Yan, C. Wang, P. Sun, G. Lu, Ultra-fast and low detection limit of H₂S sensor based on hydrothermal synthesized Cu₇S₄-CuO microflowers, Sens. Actuat. b: Chemical 350 (2022), 130847, https://doi.org/10.1016/j.snb.2021.130847.
- [26] R. Zhang, L. Gao, Q. Zhang, Photodegradation of surfactants on the nanosized TiO₂ prepared by hydrolysis of the alkoxide titanium, Chemosphere 54 (2004) 405–411, https://doi.org/10.1016/S0045-6535(03)00588-5.
- [27] M. Anpo, Use of visible light. Second-generation titanium oxide photocatalysts prepared by the application of an advanced metal ion-implantation method, Pure Appl. Chem. 72 (2000) 1787–1792, https://doi.org/10.1351/pac200072091787.
- [28] M.R.D. Khaki, M.S. Shafeeyan, A.A.A. Raman, W.M.A.W. Daud, Application of doped photocatalysts for organic pollutant degradation - A review, J. Env. Manag. 198 (2017) 78–94, https://doi.org/10.1016/j.jenvman.2017.04.099.
- [29] B. Xiao, M. Wu, Y. Wang, R. Chen, H. Liu, Sulfite activation and tetracycline removal by rectangular copper oxide nanosheets with dominantly exposed (001) reactive facets: Performance, degradation pathway and mechanism, Chem. Eng. J. 406 (2021), 126693, https://doi.org/10.1016/j.cej.2020.126693.
- [30] J. Zia, M. Ajeer, U. Riaz, Visible—light driven photocatalytic degradation of bisphenol-A using ultrasonically synthesized polypyrrole/K-birnessite nanohybrids: Experimental and DFT studies, J. Environ. Sci. 79 (2019) 161–173, https://doi.org/10.1016/j.ies.2018.11.021.
- [31] J.B. Forsyth, S. Hull, The effect of hydrostatic pressure on the ambient temperature structure of CuO, J. Phys. Condens. Matter 3 (1991) 5257–5261, https://doi.org/ 10.1088/0953-8984/3/28/001.
- [32] M.C. Biesinger, L.W.M. Lau, A.R. Gerson, R. St, C. Smart, Resolving surface chemical states in XPS analysis of first row transition metals, oxides and hydroxides: Sc, Ti, V, Cu and Zn, Appl. Surf. Sci. 257 (2010) 887–898, https://doi. org/10.1016/j.apsusc.2010.07.086.
- [33] M.C. Biesinger, B.P. Payne, B.A.P. Grosvenor, L.W.M. Lau, A.R. Gerson, R. St, C. Smart, Resolving surface chemical states in XPS analysis of first row transition metals, oxides and hydroxides: Cr, Mn, Fe, Co and Ni, Appl. Surf. Sci. 257 (2011) 2717–2730, https://doi.org/10.1016/j.apsusc.2010.10.051.
- [34] A. Khlyustova, N. Sirotkin, T. Kusova, A. Kraev, V. Titov, A. Agafonov, Doped TiO₂: the effect of doping elements on photocatalytic activity, Mater. Adv. 1 (2020) 1193–1201. https://doi.org/10.1039/D0MA00171F.
- [35] H. Faiz, K. Siraj, M.S. Rafique, S. Naseem, A.W. Anwar, Effect of zinc induced compressive stresses on different properties of copper oxide thin films, Ind. J Phys. 89 (2015) 353–360, https://doi.org/10.1007/s12648-014-0597-0.
- [36] P. S. Murthy, V. P. Venugopalan, D. D. Arunya, S. Dhara, R. Pandiyan, A. K. Tyagi, Antibiofilm activity of nano sized CuO International Conference on Nanoscience, Engineering and Technology (ICONSET 2011), 2011, pp. 580-583.
- [37] M.P. Rao, P. Sathishkumar, R.V. Mangalaraj, A.M. Asiri, P. Sivashanmugam, S. Anandan, Simple and low-cost synthesis of CuO nanosheets for visible-lightdriven, photocatalytic degradation of textile dyes, J. Environ. Chem. Eng. 6 (2018) 2003–2010, https://doi.org/10.1016/j.jece.2018.03.008.
- [38] J. Feng, L. Cheng, J. Zhang, O.K. Okoth, F. Chen, Preparation of BiVO₄/ZnO composite film with enhanced visible-light photoelectrocatalytic activity, Ceram. Int. 44 (2018) 3672–3677, https://doi.org/10.1016/j.ceramint.2017.11.124.
- [39] S. Chala, K. Wetchakun, S. Phanichphant, B. Inceesungvorn, N. Wetchakun, Enhanced visible-light-response photocatalytic degradation of methylene blue on Fe-loaded BiVO4 photocatalyst, J. Alloys Cmpds 597 (2014) 129–135, https://doi. org/10.1016/j.jallcom.2014.01.130.
- [40] A. Bhattacharjee, M. Ahmaruzzaman, CuO nanostructures: Facile synthesis and applications for enhanced photodegradation of organic compounds and reduction of p-nitrophenol from aqueous phase, RSC Adv. 6 (2016) 41348–41363, https:// doi.org/10.1039/C6RA03624D.
- [41] C. Yang, J. Wang, F. Xiao, X. Su, Microwave hydrothermal disassembly for evolution from CuO dendrites to nanosheets and their applications in catalysis and photo-catalysis, Powder Technol. 264 (2014) 36–40, https://doi.org/10.1016/j. powtec.2014.05.012.

- [42] J. Yang, Z. Li, W. Zhao, C. Zhao, Y. Wang, X. Liu, Controllable synthesis of Ag–CuO composite nanosheets with enhanced photocatalytic property, Mater. Lett. 120 (2014) 16–19. https://doi.org/10.1016/j.matlet.2014.01.026.
- (2014) 16–19, https://doi.org/10.1016/j.matlet.2014.01.026.
 [43] K. Sahu, J. Singh, S. Mohapatr, Photocatalytic and catalytic removal of toxic pollutants from water using CuO nanosheets, J. Mater. Sci: Mater. Electron. 30 (2019) 6088–6099, https://doi.org/10.1007/s10854-019-00910-3.
- [44] Z. Salmanzadeh-Jamadi, A. Habibi-Yangjeh, C. Xu, C. Wang, Anchoring Bi₄O₅I₂ and CDs on brown TiO_{2-x}: S-scheme heterojunction mechanism for impressive degradation of several antibiotics under visible light, *J. Alloys Cmpd*S. 948 (2023), 167711, https://doi.org/10.1016/j.jallcom.2023.169711.